



ORIGINAL RESEARCH ARTICLE

Numerical Investigation on the Effects of Process Parameters on the Pre-Holed Self-Piercing Riveted Joint Quality

Chao Wang, Aiguo Cheng , Wangzhen Li, Youping Sun, and Guojian Luo

Submitted: 14 May 2024 / Accepted: 2 September 2024

Although the self-piercing riveting (SPR) process is widely used in the automotive industry, it faces challenges in achieving mechanical interlock when joining high-strength steel. In this paper, the pre-holed self-piercing riveting (PH-SPR) process is adopted to join high-strength steel to aluminum alloy. This paper aims to investigate SPR joinability and select suitable rivets and dies for different steel–aluminum combinations. A 2D axisymmetric numerical model is developed using LS-DYNA commercial software to simulate the PH-SPR process with varying process parameters (e.g., rivet hardness, geometric dimensions of rivet and die, hole size, and material and thickness of sheet). The accuracy of the FE model is verified by comparing the forming quality parameters between the experimental test and the simulation result. The results show that (i) the rivet with strength of 0.9 GPa is suitable for the bottom sheet with yield stress of 89 MPa, and the rivet with strength of 1.34 GPa is appropriate for the bottom sheet with yield stress greater than 165 MPa. (ii) The increasing rivet diameter, rivet length, and hole size can improve forming quality, and the decreasing die depth and top sheet thickness can enhance the undercut. (iii) The undercut of the joint with 1.2 mm top sheet increases with the increase in yield stress of the bottom sheet, while a decreasing tendency is found for the joint with 1.6 mm top sheet. (iv) The minimum rivet length required for a successful joining increases with the increase in thickness ratio, while the opposite trend is observed for maximum rivet length.

Keywords joint quality, numerical model, pre-holed self-piercing riveting, process parameters, steel–aluminum hybrid sheets

1. Introduction

With the rapid development of lightweight vehicles, numerous lightweight materials have been applied to vehicle bodies, such as high-strength steel, aluminum alloy, and fiber reinforced polymers (CFRPs) (Ref 1). At present, the mixed usage of lightweight materials, such as steel/Al (Ref 2), Al/steel (Ref 3), and CFRP/Al (Ref 4), has become the major development trend driven by cost constraints and diverse performance requirements. However, due to the differences in physical properties between materials, the utilization of multiple materials with varying mechanical and geometrical properties poses

challenges for traditional thermal joining methods (Ref 5). As a major mechanical joining process, self-piercing riveting (Ref SPR) has been widely used to join two or more layers of dissimilar materials without the need for surface pretreatment and with low energy consumption (Ref 6). For example, Zhang et al. (Ref 7) conducted a study on the dissimilar SPR joints between aluminum–lithium alloy and titanium sheets and found that rivet hardness presented an obvious influence on the fatigue fracture path. Liu et al. (Ref 8) explored the joining mechanism and damage of SPR joints in carbon fiber reinforced polymer (CFRP) composites and aluminum alloy. Asati et al. (Ref 9, 10) proposed that the resistance spot weld (RSW) joints exhibited higher tensile-shear strength compared to SPR joints, whereas SPR joints showed significantly improved fatigue life.

The SPR joint quality of specific sheet stack generally depends on the appropriate design of process parameters, such as rivet geometry, rivet hardness, die profile, riveting velocity, etc (11). The investigation of the influences of process parameters on joint quality is beneficial to improving the stability of the SPR process and understanding the joining mechanism. Wang et al. (Ref 12) studied the effect of process parameters on mechanical responses of SPR joint, the result showed that the mechanical properties and failure mode were highly dependent on the rivet length, and larger rivet length could cause rivet fracture failure. Additionally, Wang et al. (Ref 13) also explored the effects of rivet and die parameters on crack inhibition and forming quality of SPR. It was found that the depth and diameter of the die were the main factors affecting cracking generation and forming quality. Ma et al. (Ref 14) obtained the rivetable range of a specific rivet and die

Chao Wang and **Aiguo Cheng**, State Key Laboratory of Advanced Design and Manufacturing Technology for Vehicle, Hunan University, Changsha 410082, People's Republic of China; and **Wangzhen Li**, School of Mechanical and Automotive Engineering, Guangxi University of Science and Technology, Liuzhou 545006, People's Republic of China; and Guangxi Key Laboratory of Automobile Components and Vehicle Technology, Guangxi University of Science and Technology, Liuzhou 545006, China; **Youping Sun** and **Guojian Luo**, School of Mechanical and Automotive Engineering, Guangxi University of Science and Technology, Liuzhou 545006, People's Republic of China. Contact e-mail: liwangzhen@gxust.edu.cn.

combination for the aluminum alloy and mild steel by investigating the effects of rivet hardness, rivet length, die width, and die pip height on the joinability. Jiang et al. (Ref 15) found that qualified SPR joints can be achieved by selecting the appropriate blade angle of the rivet. Asati et al. (Ref 16) studied the effects of flat die and pip die on the SPR joints, and die design significantly affected SPR output, but exhibited little effect on lap-shear load and fracture mode. On the other hand, the configuration of the sheets also significantly affects the SPR joint quality. For instance, Wang et al. (Ref 17) suggested that the SPR joinability decreased with the increase in the thickness ratio, and the SPR joinability approached zero when the thickness ratio exceeds 1.47. Ma et al. (Ref 18) employed friction SPR to join AA6061-T6 aluminum alloy and AZ31B magnesium alloy, the stack orientation of riveting from AZ31B to AA6061-T6 exhibited better forming quality and higher tensile-shear strength. Mori et al. (Ref 19) explored the joinability of three steel and aluminum alloy sheets for various combinations. The study indicated that the joinability can be improved by setting a thicker sheet as the bottom sheet. Physical experiments provide reliable test results directly, but the high cost and long duration of physical experiments limit the range of parameters that can be studied.

During recent decades, an increasing number of researchers have preferred to adopt numerical simulation techniques to predict the joint quality and study the influences of joining parameters on the joint quality rather than experimental methods. Abe et al. (Ref 20) used commercial software LS-DYNA to develop a two-dimensional (2D) axisymmetric SPR model and investigated the joinability of aluminum and steel sheets. He et al. (Ref 21) numerically simulated the SPR process using the commercial software LS-DYNA, and experimental tests were conducted to validate the accuracy of the established numerical model. Du et al. (Ref 22) constructed a 2D SPR model using the r-adaptivity method to simulate the SPR process. The design range of sheet flow stress ratio and thickness ratio for qualified SPR joints was obtained. Zhao et al. (Ref 23) investigated the influences of top sheet thickness, bottom sheet thickness, and rivet length on the joint formation mechanisms by establishing a 2D SPR model in the commercial software Simfact. Numerical simulation has significant advantages over experimental research in terms of cost and time. These advantages make numerical simulation increasingly important in the development and optimization of SPR technology.

However, the application of high-strength materials (e.g., advanced high-strength steel and ultrahigh-strength steel) can lead to the defect of ineffective mechanical interlock during the SPR process. Thus, to improve the SPR joint quality when piercing through thick and strong material sheets, several process parameter optimization and novel SPR processes have been developed and employed (Ref 24). Abe et al. (Ref 25) suggested that the high tensile strength steel sheets below 590 MPa could be successfully joined by selecting the proper rivet length ratio between rivet length and sheet thickness. Uhe et al. (Ref 26) joined two material combinations with an improved rivet geometry, rather than using different rivets before. Deng et al. (Ref 27) proposed a thermally assisted self-piercing riveting (TA-SPR) process to join aluminum to ultrahigh-strength steel. The TA-SPR joints exhibited better joint quality compared to conventional SPR joints. Zhang et al. (Ref 28) applied a laser heat treatment process to the hot-stamped steel sheet before joining. The result indicated that the

soft zone could improve joint quality by reducing sheet hardness. Ma et al. (Ref 29) developed a friction self-piercing riveting (F-SPR) process, and the rotation of rivet in F-SPR elevated the local temperature and could efficiently improve joint quality. Although the aforementioned valuable findings can improve or address the issue of riveting high-strength material, they require redesigning rivets, dies, and SPR equipment, leading to challenges such as complex processes and low universality. A simplified process utilizing conventional equipment is required to achieve the joining of high-strength steel. In the SPR joints between composites and metals, the fractured fibers can prevent the firm interlock of the rivet tail by the deformation of the metal sheet. A new technique called pre-holed self-piercing riveting (PH-SPR) is developed for joining CFRP laminates to metal sheets, demonstrating superior formability and excellent joining quality (Ref 30). Considering its stability, low cost, and simplified process characteristics, Wang et al. (Ref 31, 32) had applied the PH-SPR process to high-strength steel connections and achieved good SPR joint quality. Although previous studies have investigated the influence of process parameters on the quality of PH-SPR joints, there are still some limitations. For instance, most studies have focused on experimental methods, with relatively few numerical simulation studies. Additionally, existing research has primarily focused on the impact of individual or a few process parameters, without systematically analyzing the interactive effects of multiple parameters. Therefore, it is necessary to systematically study the influence of process parameters on the quality of PH-SPR joints using numerical simulation methods, in order to provide guidance for practical production.

In this paper, the PH-SPR process is adopted to join high-strength steel to aluminum alloy. A numerical model is developed to simulate the PH-SPR process using the commercial software LS-DYNA, and the model is verified with experimental results to prove the accuracy of the simulation. This paper aims to systematically study the process parameters of PH-SPR using numerical simulation, analyzing the influences of rivet, die, sheet, and predrilled hole diameter parameters on joint quality. Through numerical simulation, it is possible to visually observe and analyze the impact of different process parameters on the mechanical performance of joints, providing a theoretical basis for optimizing the PH-SPR process.

2. PH-SPR process and joint quality assessment

The pre-holed self-piercing riveting (PH-SPR) process is slightly modified based on the conventional self-piercing riveting (C-SPR) process, and both use the same riveting tools (Ref 30). The main difference lies in the pre-holed operation. In PH-SPR, the pre-holed operation for the top sheet is performed before the actual riveting process. The position of the pre-hole is determined by the location of the SPR joint. The PH-SPR process consists of five distinct steps, as shown in Fig.1: (1) Alignment. The rivet is placed in the pre-hole of the assembled sheet stack. The rivet and sheets are then moved together to position the rivet head into the punch channel to ensure alignment. (2) Clamping. The blank holder is driven downward to tightly clamp sheets with the die. This step ensures that the sheets are securely held in place during the subsequent steps of

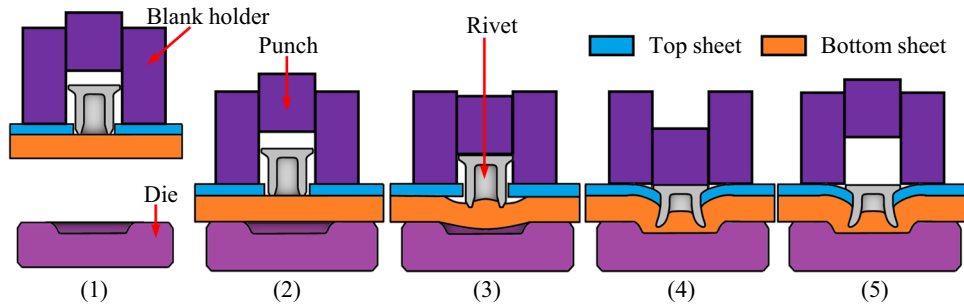


Fig. 1 Schematic illustration of the PH-SPR process

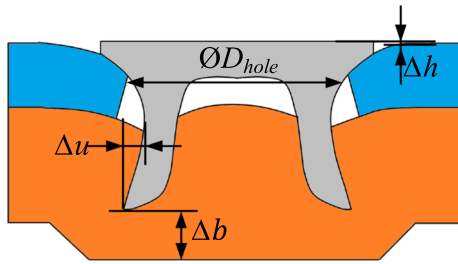


Fig. 2 Forming quality parameters of PH-SPR joint

the process. (3) Piercing. The rivet passes through the top sheet, and it only needs to pierce into the bottom sheet. Therefore, the rivet hardness is determined by the material properties of the bottom sheet. (4) Flaring. The rivet tail flares into the bottom sheet, and the mechanical interlock is formed between the sheets, providing a strong joint. The flaring of the rivet tail enhances the overall strength and stability of the joint. (5) Releasing. Once the punch reaches the predetermined position, the riveting process is considered finished.

The SPR joints require initial inspections to ensure the appearance quality, such as no cracks found on the samples and the two-layer sheets joined together. Subsequently, the geometric parameters of the joint cross-sectional profile obtained by the cutting and polishing process can be measured on the metallographic microscope. In assessing the joint quality, four key quality parameters are typically employed (Ref 11), as shown in Fig. 2: height of rivet head (Δh), undercut (Δu), bottom thickness (Δb), and hole diameter (ϕD_{hole}). The Δh needs to be controlled within a small range ($\Delta h \leq \pm 0.3$ mm) to meet the desired appearance quality. The Δu is a key indicator ($\Delta u \geq 0.2$ mm) closely related to the mechanical properties of the SPR joint. To prevent corrosion issues resulting from sheet fracture, the minimum value of Δb is usually set to 0.2 mm. Additionally, the ϕD_{hole} should be smaller than the diameter of the rivet head to ensure tight fitness.

A servo SPR system manufactured by ePRESS GmbH is selected to fabricate the SPR joints in this paper, as shown in Fig. 3(a). For effective comparison and consistency, the riveting speed is set at 100 mm/s, and the clamping force of 1.0 kN is applied on the sheets by the blank holder. A displacement control mode is adopted, which ends the riveting process when the punch reaches the predetermined displacement. The outer and inner diameters of the rivet are 5.3 mm and 3.5 mm, respectively, and the rivet length is 5.0 mm. The die with a flat bottom cavity is selected. The diameter and depth of the die are 9.0 mm and 1.2 mm, respectively. The geometrical dimensions

of the rivet and die are presented in Fig. 3(b) and (c). The diameter of the pre-hole for the top sheet is $\phi 5.5$ mm, and the hole is drilled using a bench drilling machine.

3. Numerical simulations

3.1 Material properties

In this paper, the PH-SPR joints are fabricated from high-strength steel DP590 with a thickness of 1.2 mm and die-casting aluminum AlSi10MnMg-T7 with a thickness of 3.0 mm. All the joints are made through riveting from the steel side. The rivets with a hardness of H4 are made of ultrahigh-strength steel. The mechanical properties of DP590 and AlSi10MnMg-T7 are obtained by uniaxial tensile tests using a WANCE ETM105D axial test system with a constant speed of 3 mm/min, and the digital image correlation (DIC) method is used to obtain the engineering strain of the specimens, as depicted in Fig. 4(a). In the PH-SPR process, the rivet only needs to pierce into the bottom sheet, and the effect of top sheet material on PH-SPR process is relatively small. In addition, aluminum alloy is not sensitive to strain rate according to reports (Ref 33). Thus, the influences of strain rates on high-strength steel DP590 and aluminum AlSi10MnMg-T7 are not considered. According to Du et al. (Ref 22), the compression tests of rivets are conducted to characterize the mechanical behavior of the rivet using a TSE105D axial test system, as shown in Fig. 4(b). The plastic stress–strain curves of the sheets and rivet are depicted in Fig. 5. The corresponding mechanical properties of materials are summarized in Table 1.

In order to verify the mechanical behavior of the rivet during the riveting process, the compression process of the rivet is simulated by LS-DYNA commercial software, as shown in Fig. 6(a). The FE model of the rivet is established using 8-node hexahedron solid elements, and the elastic-plastic material model (MAT24) is adopted. Figure 6(b) shows the comparison results between the test and simulation of the rivet under axial crush load, and the accuracy of the material model is verified by comparing the force–displacement curves and deformation behaviors. It can be seen that the initial stiffness and maximum force from the test and simulation are in good agreement. The compression deformation behavior of the FE model is similar to the test specimen.

3.2 Numerical model and model validation

The two-dimensional (2D) axisymmetric FE model of the PH-SPR process is established using LS-DYNA commercial

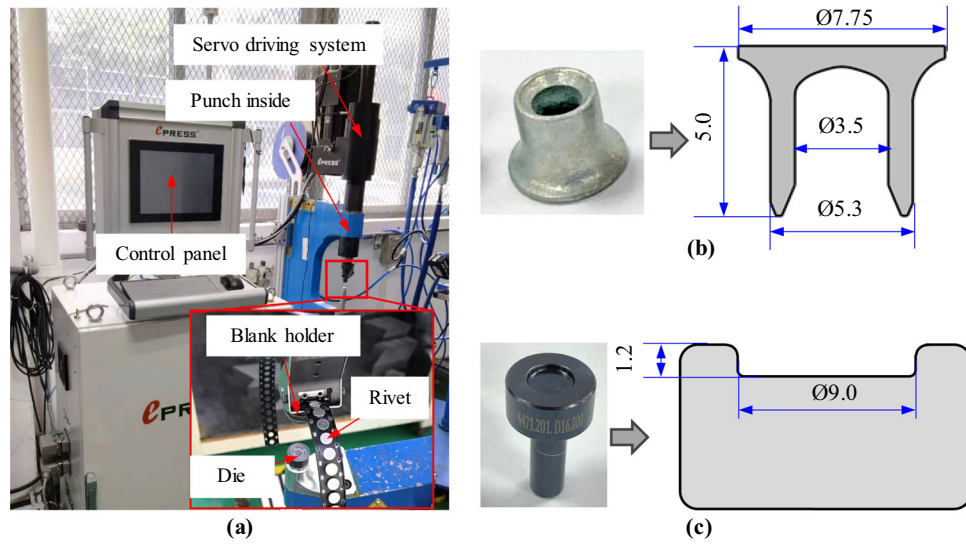


Fig. 3 Appearances and dimension parameters of the riveting tools: (a) riveting equipment, (b) semi-tubular rivets, and (c) flat die (unit: mm)

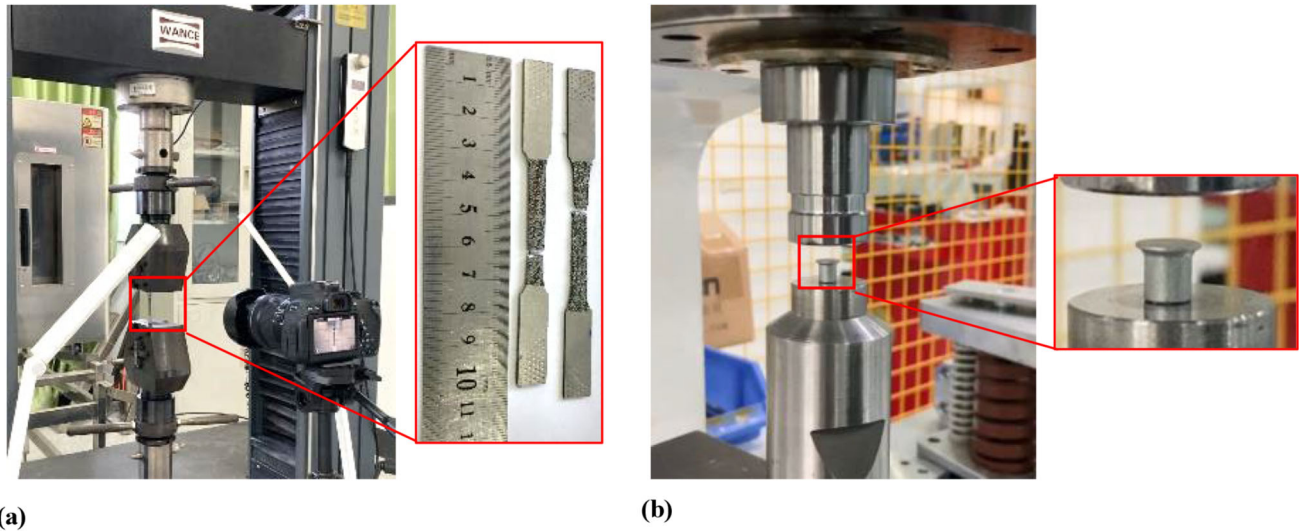


Fig. 4 Material properties of materials: (a) uniaxial tension tests for sheets and (b) axial compression test for rivet

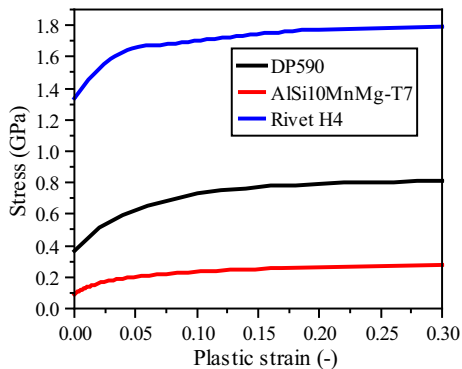


Fig. 5 Plastic stress-strain curves for sheets and rivets

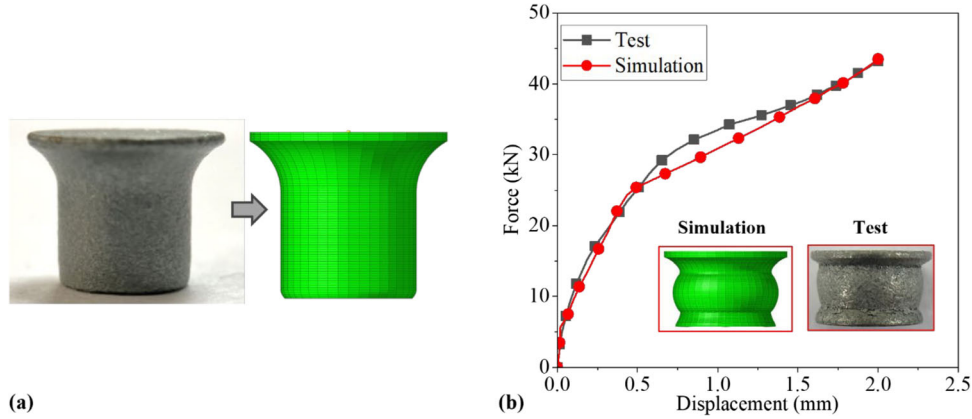
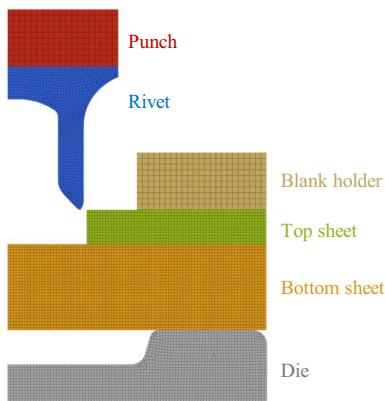
software, as shown in Fig. 7. The rivet and metal sheets are modeled using four-node 2D axisymmetric elements in LS-DYNA. To ensure accuracy, the average mesh sizes of rivet,

sheets, and die are set to $0.1 \text{ mm} \times 0.1 \text{ mm}$, while other parts are set to $0.2 \text{ mm} \times 0.2 \text{ mm}$, based on the results of the mesh sensitivity analysis (22). The r -adaptivity method is applied in the FE model to address the issue of the severe element distortion caused by the complex riveting process (Ref 22). The material models of the rivet and sheets are modeled as MAT24 according to the data in Table 1 and Fig. 5, and rigid-body material (MAT20) is selected for the punch, blank holder, and die. To account for the interaction between different components, an automatic 2D face-to-face contact algorithm with a friction coefficient of 0.2 is adopted (Ref 25). During the simulated PH-SPR process, the punch and blank holder are restricted to move only in the downward direction.

Figure 8(a) shows the comparison of the cross section shape between the experimental test and simulation result. It can be seen that the simulated shape of the PH-SPR joint shows good agreement with the tests. The undercut, bottom thickness, and hole size from the simulation are 0.523 mm, 0.586 mm, and 5.6 mm, respectively. The undercut, bottom thickness, and hole

Table 1 Mechanical properties of the materials.

| Material | Density, kg/m ³ | Young's modulus, GPa | Poisson ratio | Yield stress, MPa | Ultimate stress, MPa |
|---------------|----------------------------|----------------------|---------------|-------------------|----------------------|
| DP590 | 7.83×10^3 | 210 | 0.3 | 381 | 760 |
| AlSi10MnMg-T7 | 2.70×10^3 | 70 | 0.3 | 89 | 260 |
| Rivet H4 | 7.83×10^3 | 210 | 0.3 | 1340 | ... |

**Fig. 6** Simulation of the compression process of rivet: (a) FE model, (b) force–displacement curves**Fig. 7** Axisymmetric two-dimensional FE model of PH-SPR

size from the test are 0.497 mm, 0.627 mm, and 6.03 mm, respectively. The relative errors of forming quality parameters are within 8%. Figure 8(b) shows the SPR process simulation for various punch strokes (Δs). The rivet penetrates and flares into the bottom sheet, forming a mechanical interlock. The numerical results of the riveting process using the r-adaptivity method can avoid element distortion.

Figure 9 shows the distribution of effective strain and stress of the joint for various punch strokes (Δs). The progression of the joint can be observed through various Δs . Firstly, no bending deformation of the sheets is observed when the sheets are clamped together. Secondly, with the rivet moving downward, a slight downward bending of the sheet is found when the $\Delta s = 1.2$ mm. No evident stress and strain distribution can be observed in Fig. 9(a) and (b). Thirdly, the rivet gradually flares into the bottom sheets when the $\Delta s = 4.0$ mm. The downward movement of the rivet causes the bottom sheet to fill the die cavity, resulting in a visible gap between the top sheet and the

bottom sheet. Additionally, a significant strain concentration around the contact area with the rivet tail is found, indicating severe plastic deformation of the bottom sheet during rivet flaring. However, the rivet leg does not experience plastic deformation, because the maximum stress of the rivet leg is close to 1.2 GPa. Finally, the rivets form a mechanical interlock between the bottom sheets after the SPR process is complete. The top sheet and bottom sheet are tight fit under the action of the downward rivet head, and the gap has disappeared. The higher strain values are located under the rivet leg as a result of the strong extrusion of the bottom sheet. The rivet flaring increases the resistance between the rivet leg and the bottom sheet, which further leads to the stress of the rivet leg exceeding the yield stress. Thus, it is important to select the proper rivet size and material to ensure joint quality.

3.3 Parameter design and validation

The geometries of the rivet, sheet, and die are characterized by a series of parameters, as presented in Table 2. More specifically, the rivet is characterized by a length L_r , a cavity diameter D_r , and a yield stress S_r . The yield stress is selected to evaluate the rivet hardness, and the rivet with different hardness is simulated by translating the stress–strain curve of the rivet H4. In practical engineering applications, the commonly used Vickers hardness range for rivets is H1-H6 (280 HV10–560 HV10). The yield strength of the rivet increases with the increase in the rivet hardness. Additionally, the yield stresses of rivet H1 and rivet H6 are 0.9 GPa and 1.9 GPa, respectively (Ref 22, 23). The top sheet has a hole size D_{hole} . The die has a diameter D_d and a depth D_p . The design ranges of process parameters introduced above are listed in Table 2.

Furthermore, the effects of the material strength of the bottom sheet and sheet thickness on joint quality are also investigated. The yield stress is selected to evaluate the material strength of the sheet. Five types of aluminum alloy with

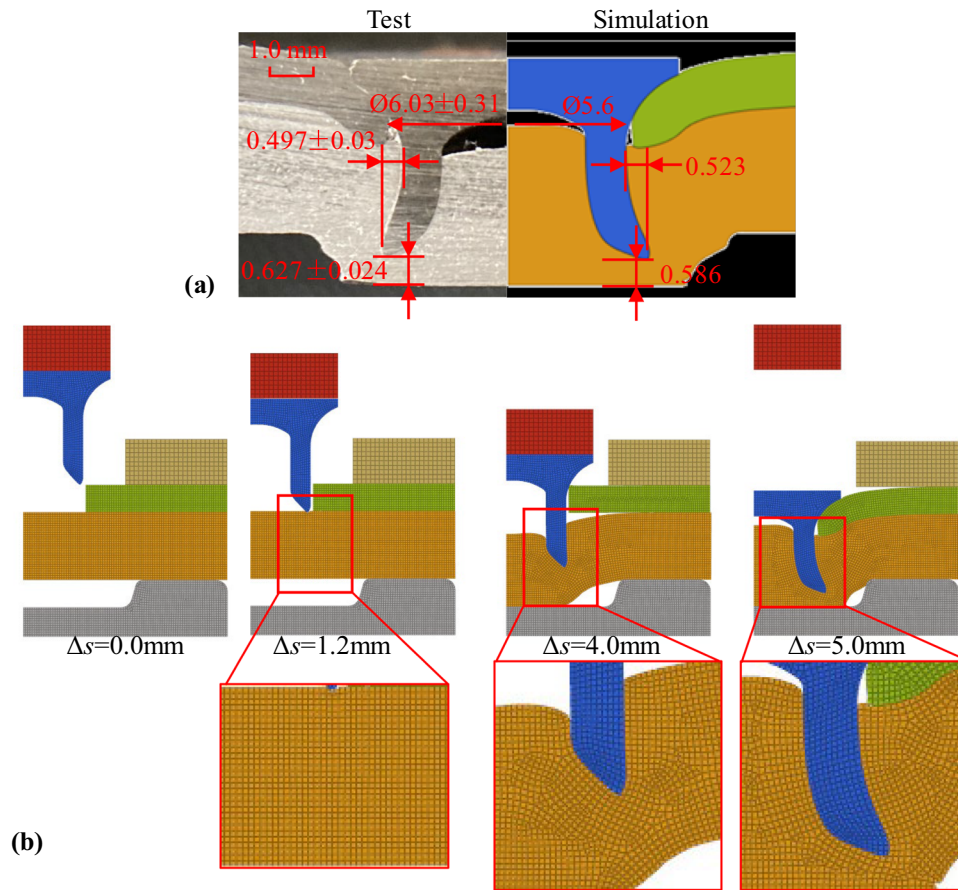


Fig. 8 Numerical simulation of SPR process: (a) the comparison of cross section between the experimental test and simulation, (b) SPR process for various punch strokes

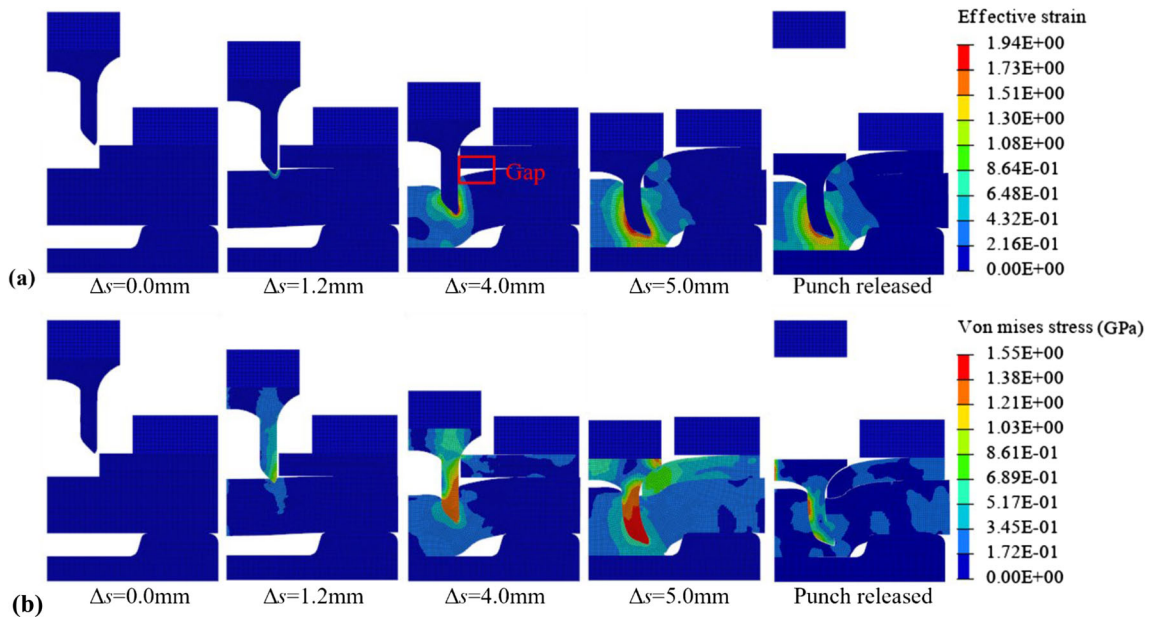


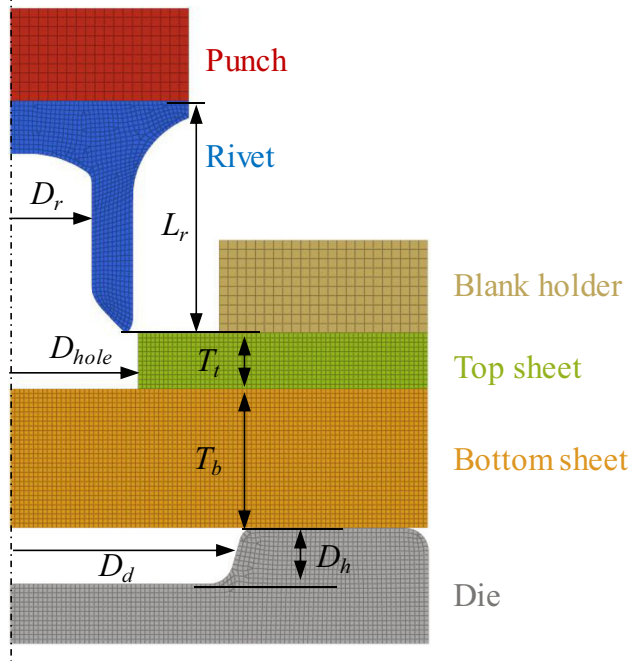
Fig. 9 The simulated results of PH-SPR joint at different punch strokes: (a) effective strain and (b) von Mises stress

different yield stress are listed in Table 3. The sheets have a yield stress of bottom sheet S_b , a top sheet thickness T_t , and a bottom sheet thickness T_b . A total of 16 sets of thickness combinations are designed for the top sheet and bottom sheet,

as shown in Table 4. The increment interval for two sheets is 0.2 mm. The thickness ratio of the top sheet to the bottom sheet denoted as R_t is defined by Eq. (1).

Table 2 The design ranges of the process parameters are specified by providing the lower and upper bounds, as well as the step size used between these bounds

| Parameters | Rivet | | | Sheet | Die | |
|--------------|---------------|---------------|---------------|-----------------|---------------|---------------|
| | L_r , mm | D_r , mm | S_r , GPa | D_{hole} , mm | D_d , mm | D_h , mm |
| Design range | 4.0: 0.5: 7.5 | 3.1: 0.2: 3.5 | 0.9: 0.1: 2.0 | 5.5: 0.5: 6.5 | 8.0: 0.5: 9.0 | 0.9: 0.3: 1.5 |



The format used is lower bound: step size: upper bound.

Table 3 Mechanical properties of sheet materials.

| Material type | Material | Young's modulus, GPa | Density, kg/m ³ | Yield stress (MPa) |
|---------------|---------------|----------------------|----------------------------|--------------------|
| Aluminum | AlSi10MnMg-T7 | 70 | 2.7×10^3 | 89 |
| | 5182-O | 70 | 2.7×10^3 | 128 |
| | 6111-T4 | 70 | 2.7×10^3 | 165 |
| | 6063-T6 | 70 | 2.7×10^3 | 245 |
| | 7075-T6 | 70 | 2.7×10^3 | 525 |

Table 4 Design range of thickness ratios.

| Parameter | Thickness, mm | | | | | | | | | | | | | | | |
|-----------|---------------|------|------|------|------|------|------|------|------|------|------|------|------|------|------|------|
| | 0.8 | 1.0 | 1.2 | 1.4 | 1.6 | 1.8 | 2.0 | 2.2 | 2.4 | 2.6 | 2.8 | 3.0 | 3.2 | 3.4 | 3.6 | 3.8 |
| T_t | | | | | | | | | | | | | | | | |
| T_b | 3.8 | 3.6 | 3.4 | 3.2 | 3.0 | 2.8 | 2.6 | 2.4 | 2.2 | 2.0 | 1.8 | 1.6 | 1.4 | 1.2 | 1.0 | 0.8 |
| R_t | 0.21 | 0.28 | 0.35 | 0.44 | 0.53 | 0.64 | 0.77 | 0.92 | 1.09 | 1.30 | 1.56 | 1.88 | 2.29 | 2.83 | 3.60 | 4.75 |

$$R_t = \frac{T_t}{T_b} \quad (\text{Eq 1})$$

In order to ensure the accuracy of parametric study, five sets of parameters are selected for verification, and the parameter values are listed in Table 5. These parameters include rivet

length, rivet strength, die size, bottom sheet material, and top sheet thickness. The experimental tests and simulated results in Fig. 10 indicate that the developed numerical model can simulate different process parameters. Thus, the developed FE model of the PH-SPR process can be used for parametric study.

Table 5 The comparison of forming quality parameters of SPR joints with different joining parameters.

| Process parameters | | J1 | J2 | J3 | J4 | J5 |
|--------------------|-------------------|---------------|---------------|---------|---------------|---------|
| Top sheet | Thickness, mm | 1.2 | 1.2 | 1.2 | 1.6 | 1.6 |
| | Material | DP590 | DP590 | DP590 | DP590 | DP590 |
| Bottom sheet | Thickness, mm | 3.0 | 3.0 | 3.0 | 3.0 | 3.0 |
| | Material | AlSi10MnMg-T7 | AlSi10MnMg-T7 | 6063-T6 | AlSi10MnMg-T7 | 6063-T6 |
| Rivet | Length, mm | 5.5 | 5.0 | 5.0 | 5.0 | 5.0 |
| | Yield stress, GPa | 1.34 | 1.9 | 1.34 | 1.34 | 1.34 |
| Die | Diameter, mm | 9.0 | 9.0 | 9.0 | 9.0 | 9.0 |
| | Depth, mm | 1.2 | 1.2 | 1.2 | 0.8 | 1.2 |

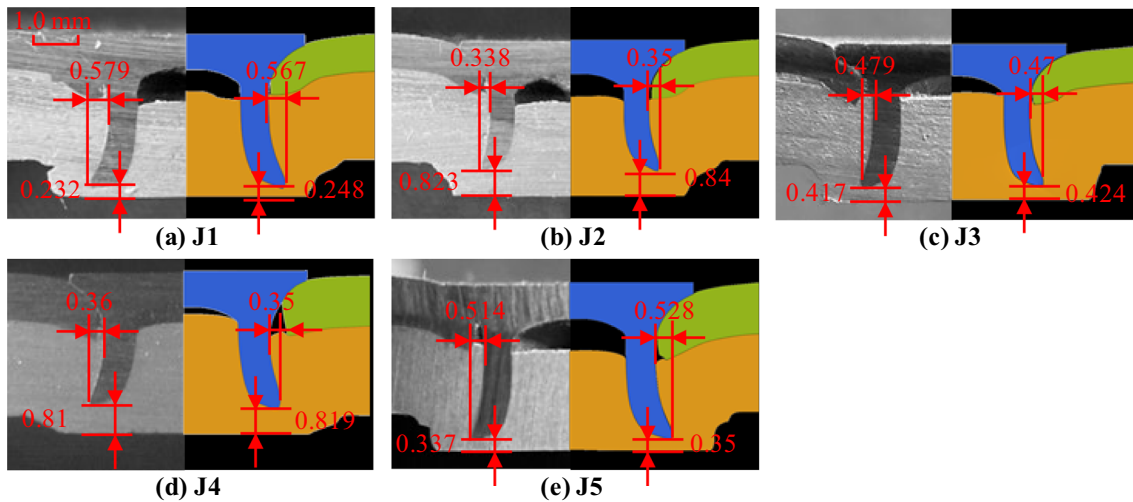


Fig. 10 The comparison of cross section of SPR joints with different joining parameters

4. Parametric study

4.1 Influences of rivet strength and yield stress of bottom sheet

In this section, three different materials of the bottom sheet (S_b) are simultaneously simulated to account for the differences in the rivet piercing into the bottom sheet. Figure 11 shows the results of the influences of rivet strength (S_r) on forming quality parameters when the other process parameters are kept fixed. When the S_r increases from 900 MPa to 2000 MPa, the variation trend of the undercut can be divided into two types, as shown in Fig. 11(a). The undercut decreases with the increase in the S_r when the yield stress of the bottom sheet is 89 MPa. However, when the S_r increases from 900 MPa to 1200 MPa, the undercut of the joint with the S_b larger than 165 MPa demonstrates an increasing trend and then keeps constant, but a decreasing tendency when the S_r is greater than 1600 MPa. For bottom sheets with lower yield stresses, a rivet with lower yield stress performs better and can enhance joint quality. Conversely, for higher yield stress sheets, increasing the rivet strength is necessary to achieve optimal joint quality. The variation trend of each curve of bottom thickness is basically the same, as shown in Fig. 11(b). The bottom thickness decreases gradually with the increase in the S_r . This uniform trend across all material types indicates that higher rivet strength causes more significant thinning of the bottom sheet,

likely due to increased compressive forces during the riveting process. The findings indicate a complex interaction between S_r and S_b , and selecting an appropriate rivet strength is crucial for optimizing joint quality.

To assist the contour graph analysis, Fig. 12 shows the distribution of stress and effective strain of the joints when using rivets with hardness levels H1 and H6, respectively, and a bottom sheet yield stress of 89 MPa. Both types of rivets are capable of forming interlock with the bottom sheet, as shown in Fig. 12(a) and (b). However, rivet H6 exhibits a deeper penetration into the bottom sheet and a smaller undercut compared to rivet H1. This can be attributed to the fact that rivets with higher hardness are less prone to deformation. Additionally, there is a larger gap between the head of rivet H1 and the top sheet compared to rivet H6. The difference occurs due to the outward movement of the bottom sheet material caused by the flaring of the rivet leg during the riveting process. It is worth noting that the maximum stress experienced by both types of rivets exceeds their respective yield stress. Specifically, rivet H1 exceeds its yield stress by 32%, while rivet H6 exceeds it by 7.3%. The plastic deformation of the bottom sheet on rivet H6 is more obvious than that of rivet H1, as shown in Fig. 12(c) and (d). Due to the more pronounced compression caused by the rivet tail of rivet H6 approaching the bottom sheet, there is an increased plastic strain on the bottom sheet, which poses a risk of sheet fracture.

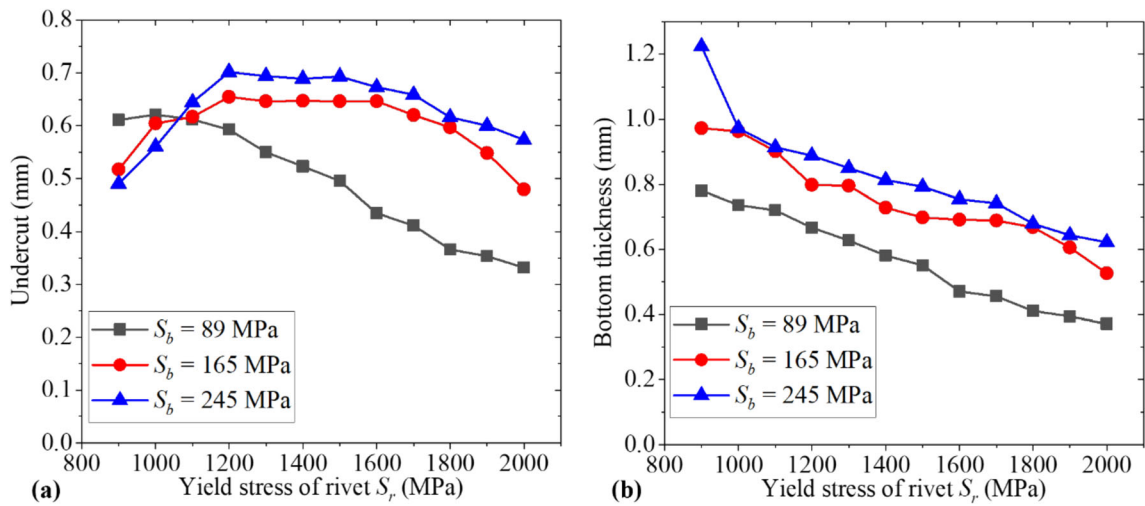


Fig. 11 The effects of varying S_r on (a) the undercut and (b) bottom thickness

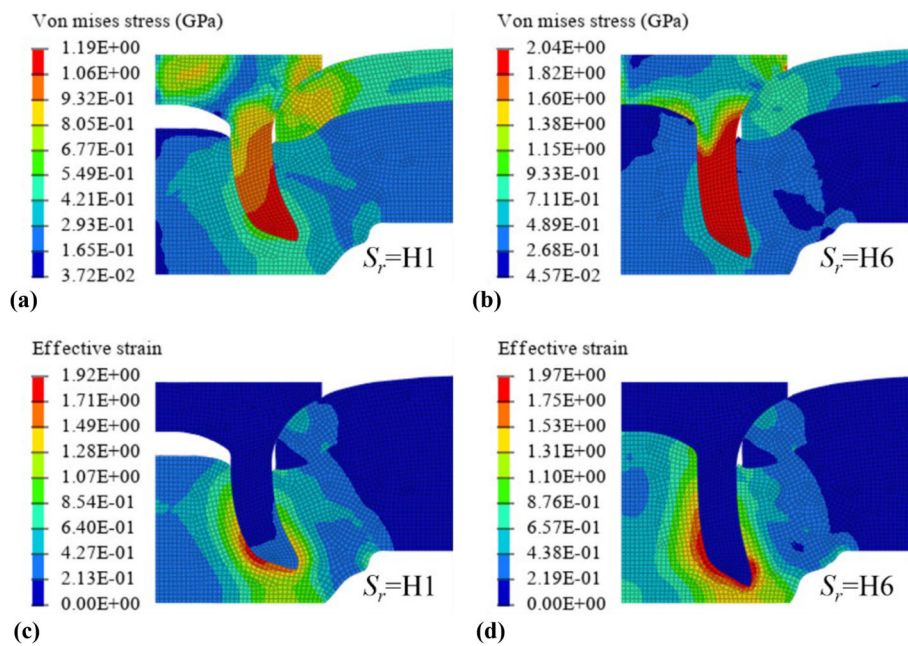


Fig. 12 Distribution of stress and effective strain of SPR joints with different rivet hardness: (a) and (c) $S_r = H1$, (b) and (d) $S_r = H6$

4.2 Influences of rivet length, die depth, and die diameter

When the rivet hardness is fixed at H4, the contour graphs of undercut and bottom sheet thickness with different rivet lengths (L_r), die depths (D_h), and die diameters (D_d) are depicted in Fig. 13. As shown in Fig 13(a) and (b), increasing the L_r from 4.5 mm to 6.0 mm enhances the undercut, which is crucial for achieving a secure mechanical interlock. However, this also results in a reduction in the bottom thickness, potentially compromising the structural integrity if it becomes too small. Conversely, reducing the D_h similarly improves the undercut while maintaining an adequate bottom thickness. This suggests that optimizing D_h can be a strategy to balance the need for a sufficient mechanical interlock without excessively reducing the bottom thickness. The nonparallel lines in Fig. 13(c) and (d) show evident interaction effects between the L_r and D_d . For a given die diameter, an increase in L_r results in an increase in

undercut and a decrease in bottom thickness. This interaction becomes more pronounced as the D_d exceeds 8.5 mm, where the rate of increase in undercut with respect to L_r becomes more substantial. When D_d is equal to 8.0 mm, the undercut shows a slower increasing tendency. This suggests that smaller D_d provides more consistent undercut behavior across different L_r , which could be useful in applications requiring uniform performance. With the D_d increasing from 8.0 to 8.5 mm, the undercut shows an increasing trend when the L_r is larger than 5.5 mm, and less effect on the undercut is found when the L_r is smaller than 5.0 mm. Additionally, the bottom thickness shows an increasing tendency as the L_r increases from 4.5 to 6.0 mm. The analysis indicates that the bottom thickness is relatively stable when D_d ranges from 8.0 mm to 9.0 mm, and increasing the D_d is an effective way to improve the joint quality.

Figure 14 illustrates the distribution of stress and effective strain of the joints when the die depths are 0.9 mm and

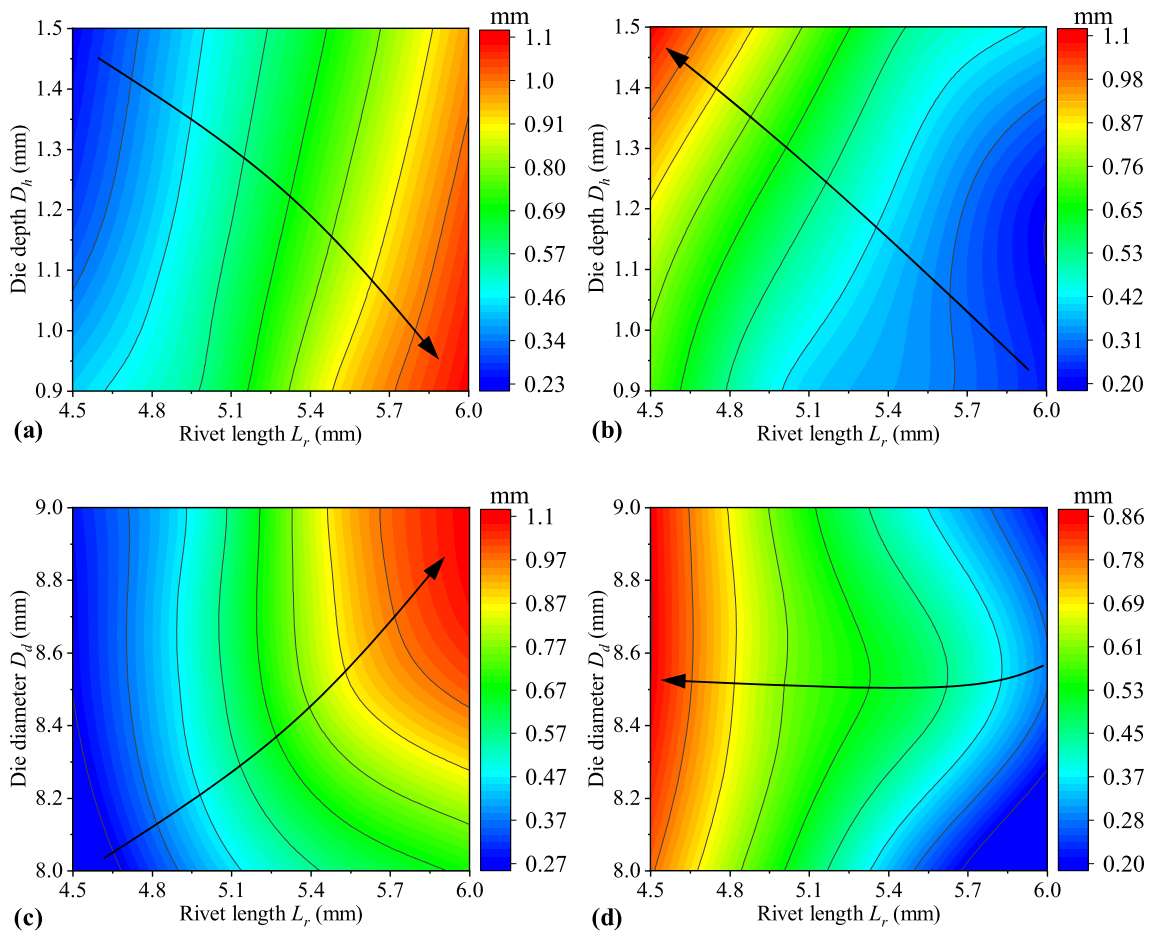


Fig. 13 Contour graphs of (a) the undercut and (b) the bottom thickness with different D_h and L_r , and contour graphs of (c) the undercut and (d) the bottom thickness with different D_d and L_r

1.5 mm, respectively. It can be concluded that increasing die depth can reduce the maximum stress on the rivet leg and effective strain on the bottom sheet. Furthermore, the smaller bottom thickness provides a larger supporting force to drive the rivet flaring. Due to the increasing die cavity, more materials from the bottom sheet are extruded into the die cavity, resulting in an increasing gap between the rivet head and the bottom sheet, as shown in Fig. 14(a) and (b). The rivet leg is fully flared into the bottom sheet, leading to a larger contact area and increasing resistance between the rivet leg and bottom sheet when the die depth is 0.9 mm, as depicted in Fig. 14(a). Thus, the stress on the rivet leg increases by 2.6% compared to the result in Fig. 7(b). The smaller bottom thickness indicates the severe distortion of the bottom sheet, which leads to an increase in effective strain by 12.4% compared to the result in Fig. 7(a), as shown in Fig. 14(c). However, the opposite results are found when the die depth is 1.5 mm, as shown in Fig. 14(b) and (d).

When the die depth is fixed at 1.2 mm, the numerical results of the joints with different die diameters and rivet lengths are shown in Fig. 15. Once the die cavity is fully filled, the side wall of the die will provide a high resistance force to prevent further flaring of the rivet (Ref 34). Thus, a smaller undercut can be observed when the die diameter is 8.0 mm, as shown in Fig. 15(a) and (b). Although the rivet leg is fully flared into the bottom sheet when the die diameter is 8.0 mm and the rivet length is 5.0 mm, a decreasing trend is found in both the stress

on the rivet leg and effective strain on the bottom sheet, which is opposite to the result in Fig. 14(a) and (c), as shown in Fig. 15(a) and (d). This is because the smaller die depth results in the earlier comprehensive contact between the rivet leg and bottom sheet during the riveting process, as illustrated in Fig. 16. As the rivet length increases to 5.5 mm, the rivet tail is close to the die profile, leading to the severe distortion of the bottom sheet and the increasing effective strain on the bottom sheet, as shown in Fig. 15(b) and (e). However, when the die diameter is 9.0 mm and the rivet length is 5.5 mm, smaller stress on the rivet leg and effective strain on the bottom sheet are observed in Fig. 15(c) and (f) due to the larger die cavity. The above results demonstrate that the size of the die cavity plays a crucial role in determining the stress distribution and deformation behavior of the joint components.

Figure 17 depicts the simulated results of the joint when the rivet length and die depth are 6.0 mm and 1.2 mm, respectively. It can be found that the longer rivet can improve the undercut and increase the risk of sheet fracture. Although a larger undercut can be achieved due to evident rivet flaring, the bottom thickness reaches the minimum value of 0.2 mm. Compared to the results in Fig. 7, the maximum stress on the rivet leg and effective strain on the bottom sheet increase by 17.4% and 28.6%, respectively. The higher effective strain is observed under the rivet tail, which indicates the high risk of sheet fracture.

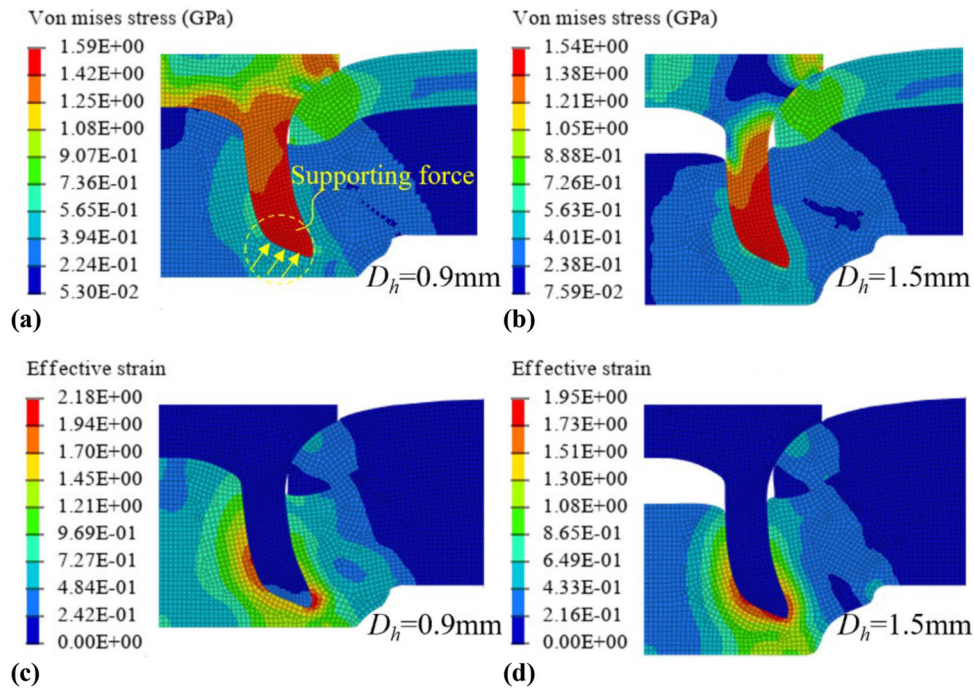


Fig. 14 Distribution of stress and effective strain of SPR joints: (a) and (c) $D_h = 0.9$ mm and (b) and (d) $D_h = 1.5$ mm

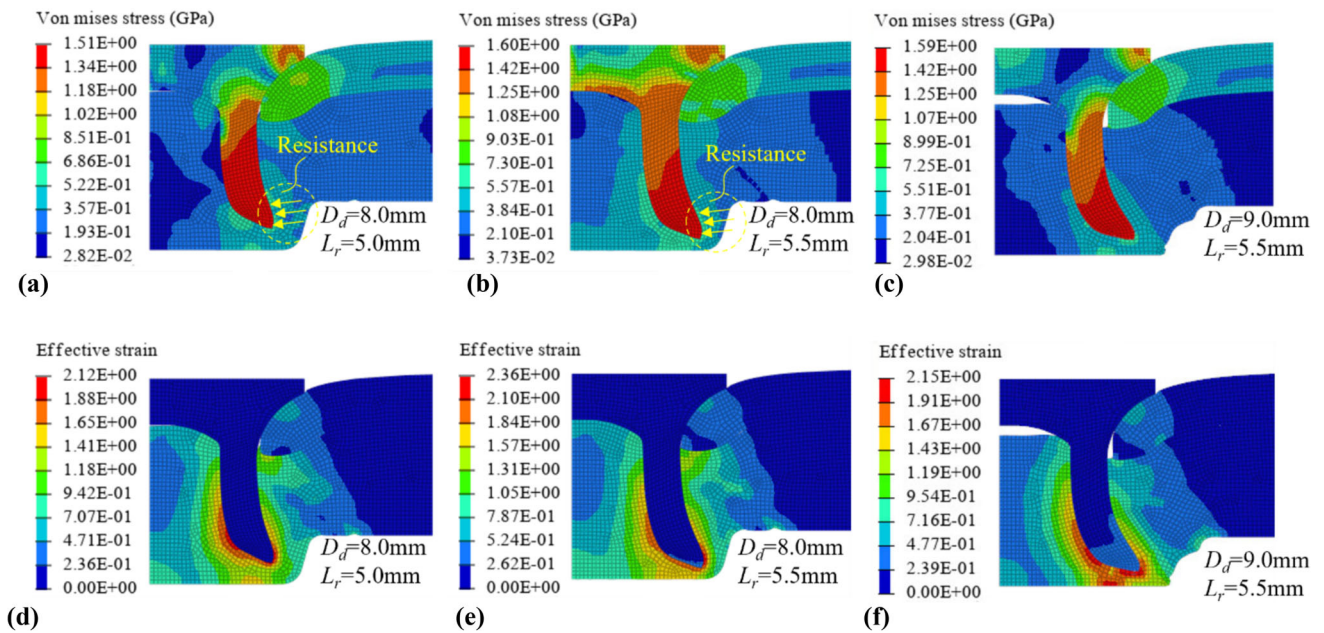


Fig. 15 Distribution of stress and strain of SPR joints: (a) and (d) $D_d = 8.0$ mm, $L_r = 5.0$ mm, (b) and (e) $D_d = 8.0$ mm, $L_r = 5.5$ mm, and (c) and (f) $D_d = 9.0$ mm, $L_r = 5.5$ mm

4.3 Influences of top sheet thickness and hole size

When the parameters of rivet and die remain constant, the interaction between varying top sheet thicknesses (T_t) and hole sizes (D_{hole}) on undercut and bottom thickness can be observed through the contour graphs in Fig. 18. Evident interaction effects between the T_t and D_{hole} on the undercut are found by the nonparallel lines, as shown in Fig. 18(a). With the D_{hole} increasing from 5.5 to 6.5 mm, the undercut increases at a higher rate with a thinner top sheet (e.g., $T_t = 0.8$ mm) compared to a thicker top sheet (e.g., $T_t = 1.6$ mm). When

the T_t increases from 0.8 to 1.6 mm, a higher decreasing rate of the undercut is found when the D_{hole} is 6.5 mm. This suggests that the D_{hole} has a more pronounced effect on the undercut when the top sheet is thinner. As shown in Fig. 18(b), the effect of D_{hole} on bottom thickness is relatively weak. The gradients remain consistent with the increase in D_{hole} , suggesting that variations in D_{hole} do not significantly affect the bottom thickness. An increasing trend is found in the bottom thickness when the T_t increases from 0.8 to 1.6 mm. The results indicate that the larger hole size can improve the joint quality. The

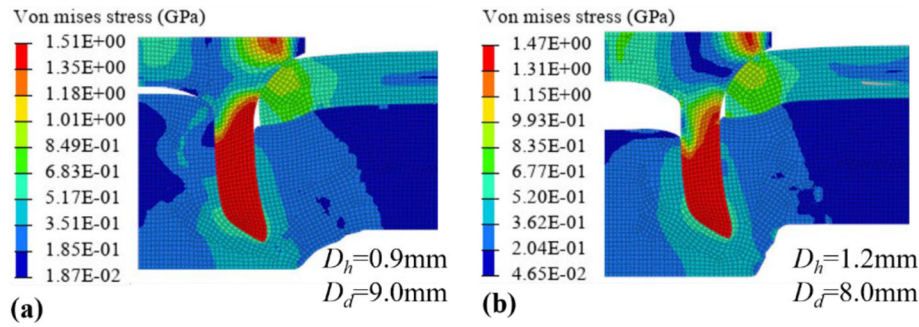


Fig. 16 Distribution of stress of SPR joints with $\Delta S = 4.5$ mm: (a) $D_h = 0.9$ mm, $D_d = 9.0$ mm and (b) $D_h = 1.2$ mm, $D_d = 8.0$ mm

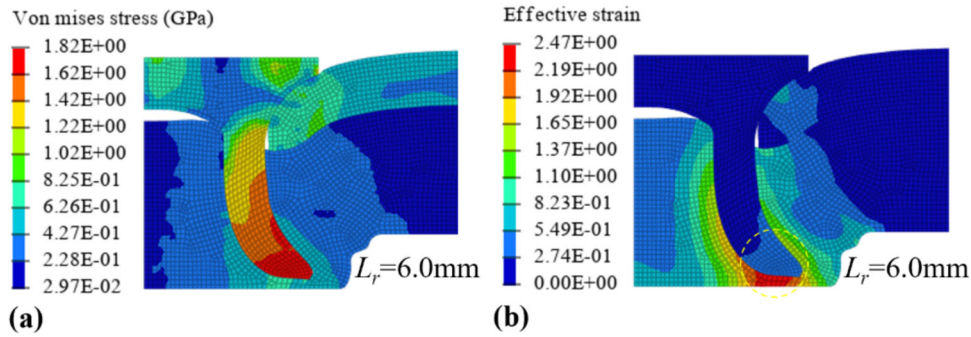


Fig. 17 Distribution of stress and effective strain of SPR joint with a 6.0 mm rivet length

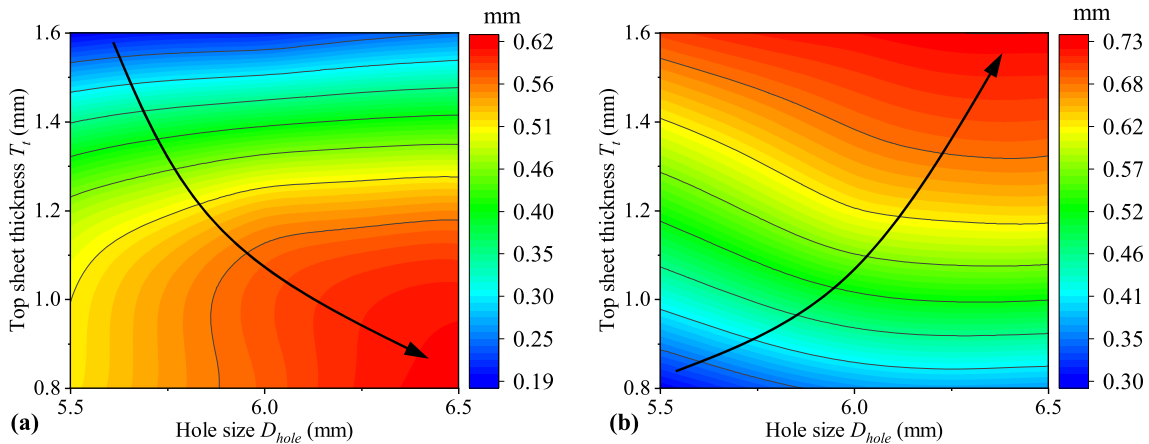


Fig. 18 Contour graphs of (a) the undercut and (b) the bottom thickness with different T_t and D_{hole}

results indicate that a larger D_{hole} can improve joint quality by enhancing the undercut, particularly for thinner top sheets. However, the increased T_t can reduce the sensitivity of the undercut to changes in D_{holes} , providing a more stable performance.

The hole sizes after riveting with different top sheet thicknesses and initial hole sizes are shown in Fig. 19(a). It can be concluded that the hole size before and after riveting is influenced by the top sheet thickness and the initial hole size. An increasing trend of hole size before and after riveting is observed when the top sheet thickness is 0.8 mm. However, when the top sheet thickness is larger than 1.2 mm, the hole size after riveting is basically equal to the initial hole size. Additionally, it is found that the hole size increases more significantly when the initial hole size is smaller (e.g.,

$D_{hole} = 5.5$ mm) compared to the larger initial hole size (e.g., $D_{hole} = 6.5$ mm). The results can be explained by considering the bending deformation of a cantilever beam, as shown in Fig. 19(b). In this analogy, the position of the hole can be approximated as the free end, and the position under the blank holder can be approximated as the fixed end. The top sheet around the hole experiences bending deformation under the action of the downward rivet. The larger bending deformation can cause greater variation in hole size before and after riveting. The increase in top sheet thickness can enhance the stiffness of the top sheet which further reduces the bending deformation. The increase in hole size will reduce the length of the cantilever, leading to a decrease in bending deformation.

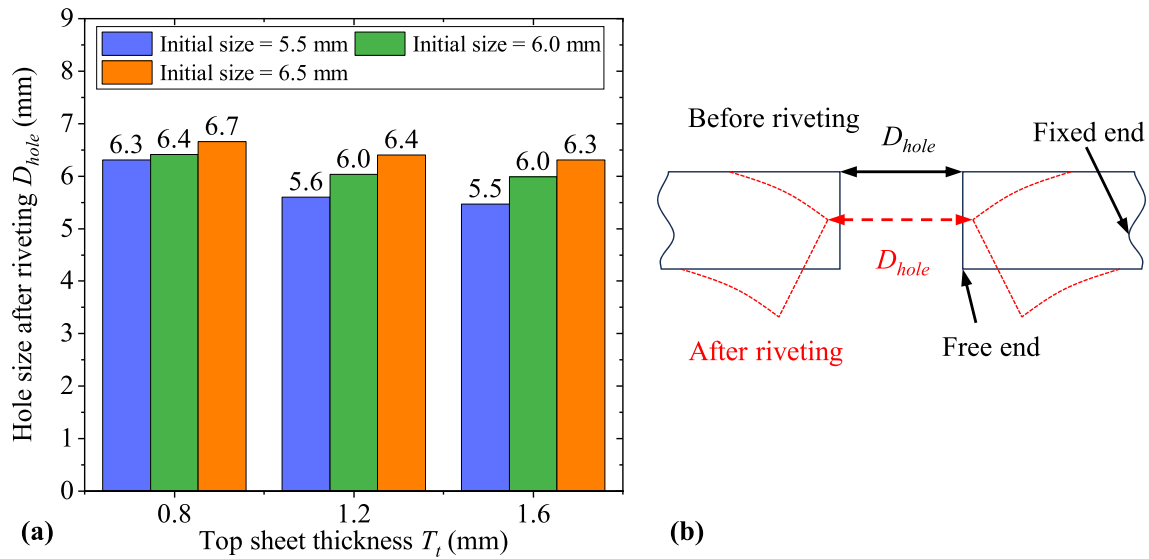


Fig. 19 (a) The value of D_{hole} after riveting and (b) schematic illustration of the deformation of the hole

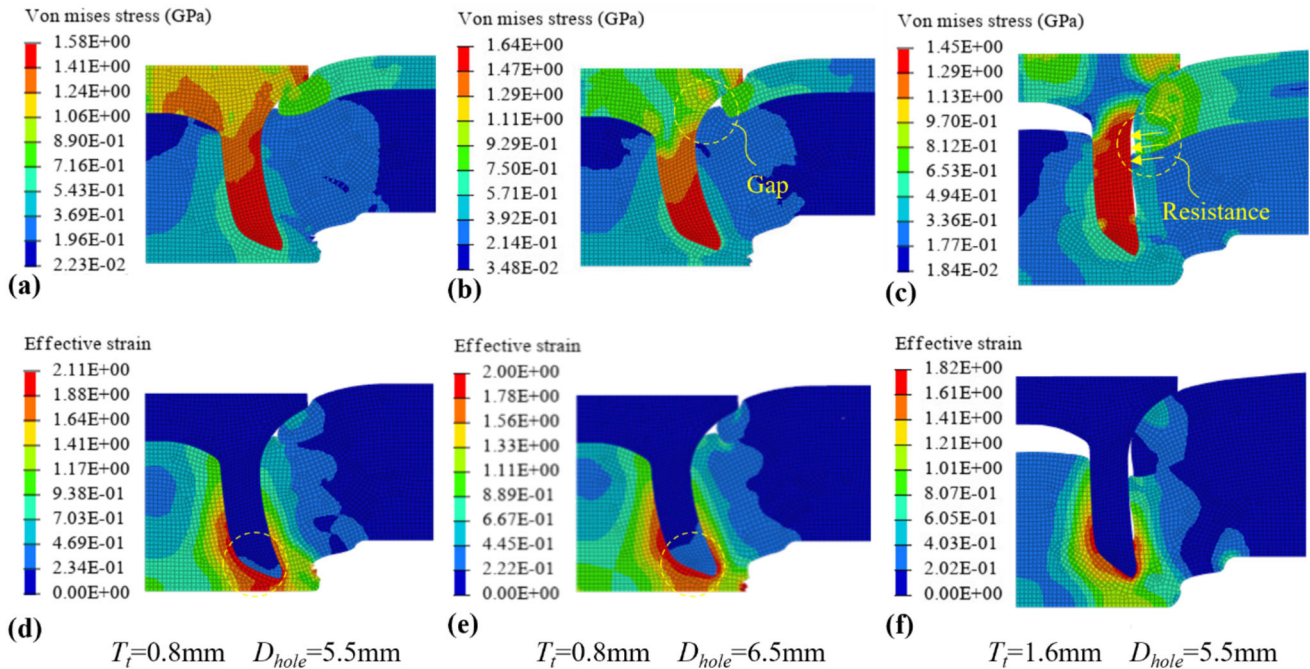


Fig. 20 Distribution of stress and effective strain of SPR joints: (a) and (d) $T_t = 0.8$ mm, $D_{hole} = 5.5$ mm, (b) and (e) $T_t = 0.8$ mm, $D_{hole} = 6.5$ mm, and (c) and (d) $T_t = 1.6$ mm, $D_{hole} = 5.5$ mm

Figure 20 shows the simulated results of the joints with different hole sizes and top sheet thickness. Compared to the top sheet with a thickness of 1.2 mm in Fig. 7, the top sheet with a thickness of 0.8 mm allows the deeper penetration of the rivet into the bottom sheet, as shown in Fig. 20(a) and (b). Thus, an increase in undercut and a decrease in bottom thickness are observed. Moreover, the contact surface between the rivet leg and the bottom sheet expands, resulting in an increase in stress on the rivet leg and effective strain on the bottom sheet, as shown in Fig. 20(a), (b), (d), and (e). A high risk of sheet fracture arises due to the severe concentration of strain under the rivet tail. When the hole size increases from 5.5

to 6.5 mm, the larger hole size enables material from the bottom sheet to flow into the gap between the rivet leg and the top sheet. This allows the rivet to flare more freely, leading to a larger undercut, as depicted in Fig. 20(b). Meanwhile, the thicker top sheet reduces the length of rivet piercing, and the top sheet provides resistance force to prevent further flaring of the rivet, resulting in a smaller undercut and bottom thickness, as shown in Fig. 20(c). The reduction in the length of rivet piercing further contributes to the decrease in stress on the rivet leg and effective strain on the bottom sheet, and an apparent gap between the rivet head and bottom sheet can be found in Fig. 20(c) and (f).

4.4 Influences of yield stress of bottom sheet and top sheet thickness

The effects of the yield stress of the bottom sheet (S_b) on joint quality, considering two different top sheet thicknesses (T_t), are plotted in Fig. 21. Figure 21(a) shows that the undercut of a joint with a T_t of 1.2 mm is greater than that of a joint with a T_t of 1.6 mm. This indicates that a thinner top sheet can lead to a more pronounced mechanical interlock. Two varying trends can be found in Fig. 21(a): when the T_t is 1.6 mm, the undercut decreases with the increase in S_b . In contrast, when the T_t is 1.2 mm, a higher increasing trend is found in the early stage, followed by a slower increasing trend in the later stage. Understanding the interaction between the T_t and S_b is vital for optimizing joint quality. Furthermore, it can be seen that the variation trend of the bottom thickness with different top sheet thicknesses is basically the same, as shown in Fig. 21(b). The bottom thickness increases with the increase in T_t , and the larger T_t can enhance the bottom thickness. The results suggest achieving a balance between top sheet thickness and the yield stress of the bottom sheet is crucial. Selecting appropriate rivet parameters for various T_t and S_b combinations can help to meet specific performance requirements.

To explain the varying trend of undercut, three simulated results with different parameters are shown in Fig. 22. The increasing yield stress of the bottom sheet can cause an increase in stress on the rivet leg when the top sheet thickness is 1.2 mm, as shown in Fig. 22(a) and (b). However, small variations of effective strain on the bottom sheet are observed, as shown in Fig. 22(d) and (e). This is because the bottom sheet experiences less compression from the rivet. The larger material strength provides greater supporting force to drive the rivet to upset and flare, resulting in a larger undercut and bottom thickness. Moreover, the root of the rivet leg experiences flaring deformation. In contrast, when the top sheet thickness is 1.6 mm, the decreasing trends in stress on the rivet leg and effective strain on the bottom sheet are found in Fig. 22(c) and (f). This is still because of the reduction in the length of rivet piercing. The difference in undercut may be attributed to the different deformation of the root of the rivet leg. The thicker top sheet exerts high resistance on the root of the rivet leg, and the rivet leg still maintains a straight shape. Under the circumstances, the increase in the yield stress of the bottom sheet

further adds resistance to the rivet leg, which prevents the flaring rivet.

4.5 Influences of rivet length and sheet thickness ratio

Four statuses of the PH-SPR process are adopted to assess the effects of rivet lengths (L_r) and sheet thickness ratios (R_t) on forming quality, as shown in Fig. 23. A successful joining of the PH-SPR joint should meet the requirements of forming quality parameters, as shown in Fig. 23(a). The following three defects mean the failed joining of the PH-SPR joint. The small Δu indicates insufficient mechanical interlock, as shown in Fig. 23(b). The smaller Δu may cause the bottom sheet fracture on the joint button, as shown in Fig. 23(c). Figure 23(d) shows the mixed status of the two defects described above.

Figure 24 shows the joint quality matrix for varying rivet lengths and sheet thickness ratios. When the thickness ratio exceeds 1.3, no successful joints are observed, and the range of successful joining reduces with the increase in thickness ratio. This indicates a critical threshold beyond which the joint quality deteriorates significantly. With the thickness ratio increasing from 0.21 to 0.35, successful joining can be achieved with rivet lengths between 4.5 and 7.0 mm. Specifically, a maximum thickness ratio of 1.3 can be achieved with a rivet length of 5.5 mm. As the thickness ratio increases, the required rivet lengths for successful joining become more restrictive. Specifically, the minimum rivet length required for a successful joint increases, while the maximum rivet length decreases. This narrowing window suggests that higher thickness ratios demand more precise rivet length selection to achieve acceptable joint quality. However, when the rivet length is either 4.0 mm or 7.5 mm, all joints fail to achieve successful joining. Rivet lengths of 4.0 mm or shorter consistently result in joint failure due to inadequate mechanical interlock. When the thickness ratio is less than 1.88, the larger rivet length tends to cause the sheet fracture on the joint button, and the mixed status of insufficient mechanical interlock and sheet fracture is observed when the thickness ratio and rivet length are greater than 1.88 and 5.0 mm, respectively. In conclusion, the interaction between rivet length and sheet thickness ratio is crucial for determining joint quality. Specifically, maintaining thickness ratios below 1.3 and selecting rivet lengths within the identified optimal ranges can enhance joint reliability and performance.

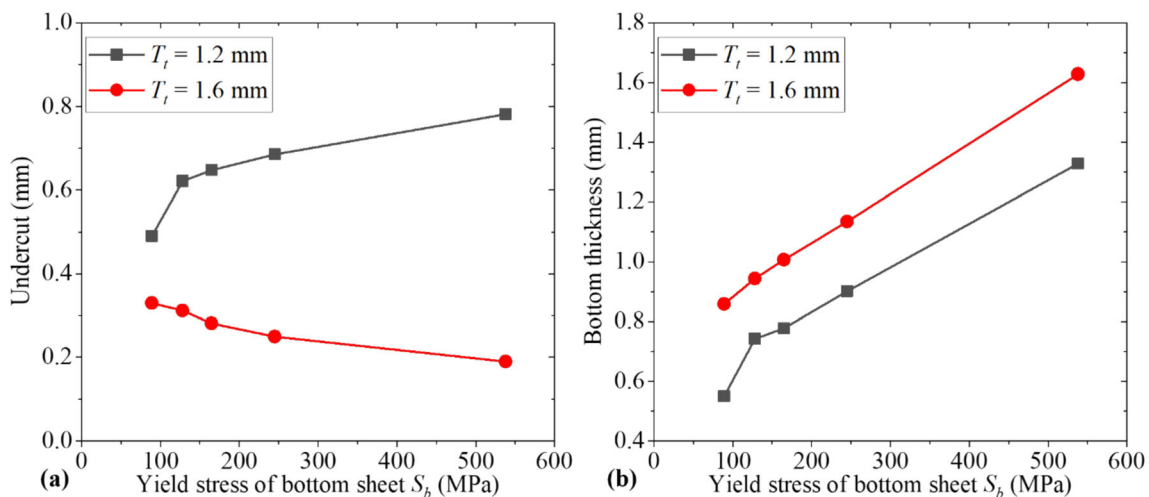


Fig. 21 The effects of varying S_b on (a) the undercut and (b) bottom thickness

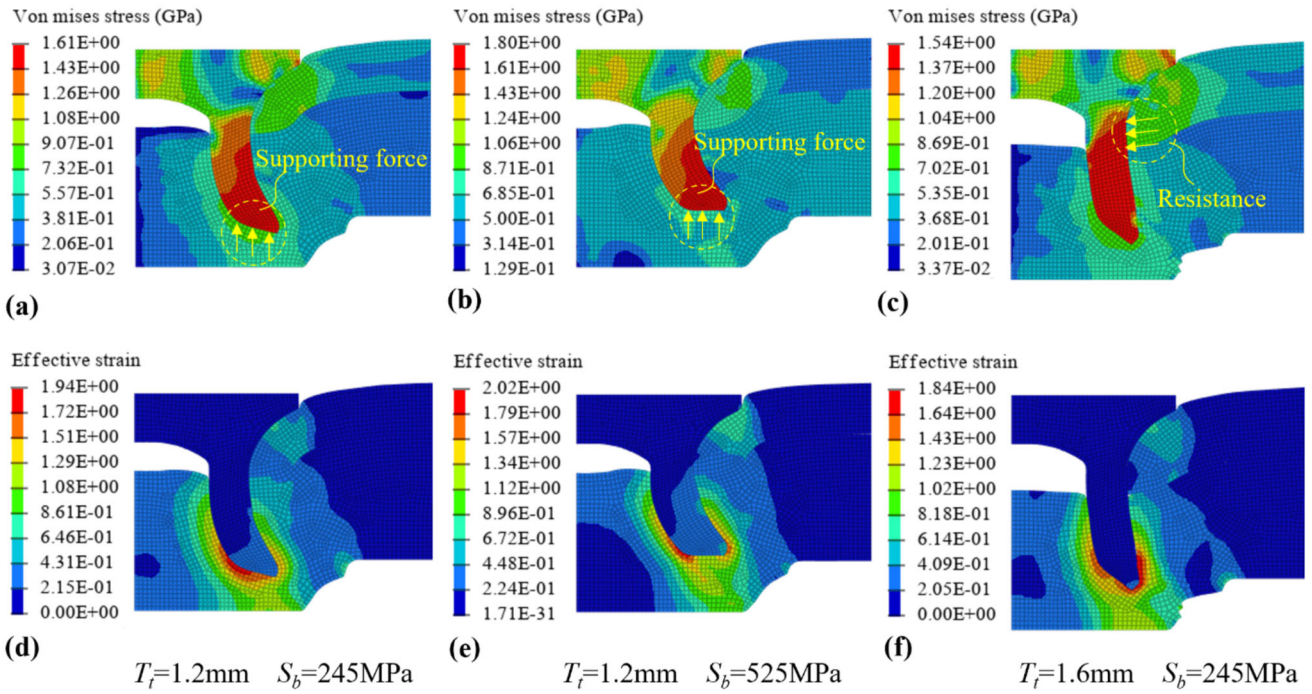


Fig. 22 Distribution of stress and effective strain of SPR joints: (a) and (d) $T_t = 1.2$ mm, $S_b = 245$ MPa, (b) and (e) $T_t = 1.2$ mm, $S_b = 525$ MPa, and (c) and (d) $T_t = 1.6$ mm, $S_b = 245$ MPa

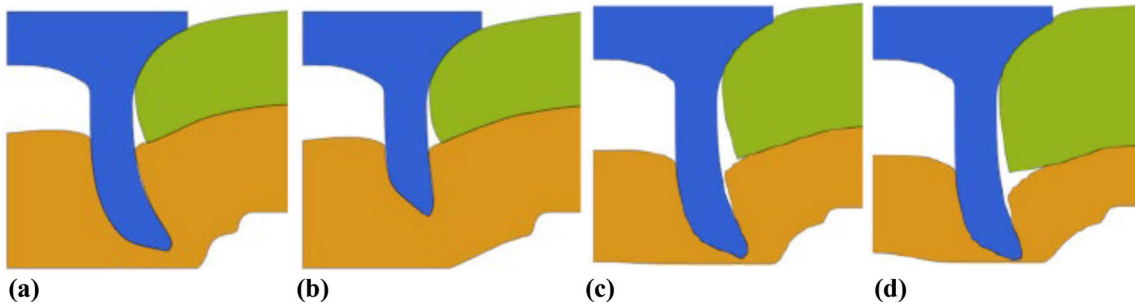


Fig. 23 Four statuses of the PH-SPR process: (a) successful joining, (b) small Δu , (c) small Δb , (d) small Δu and small Δb

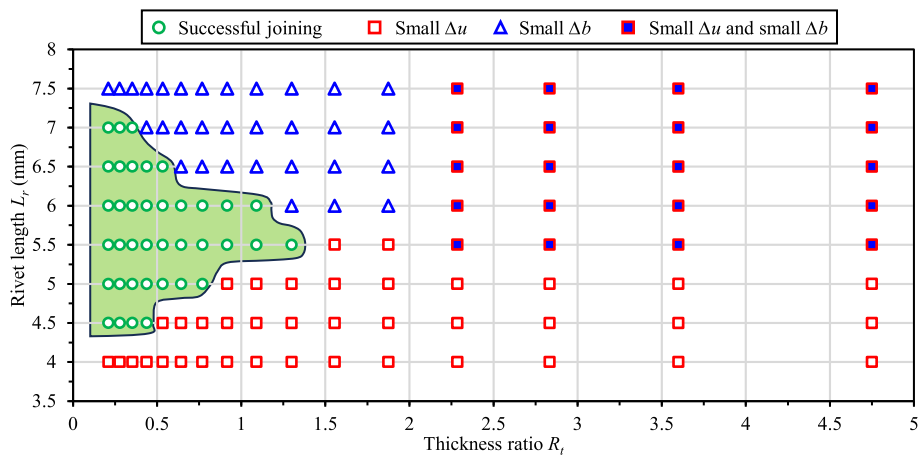


Fig. 24 The joint quality matrix with different R_t and L_r .

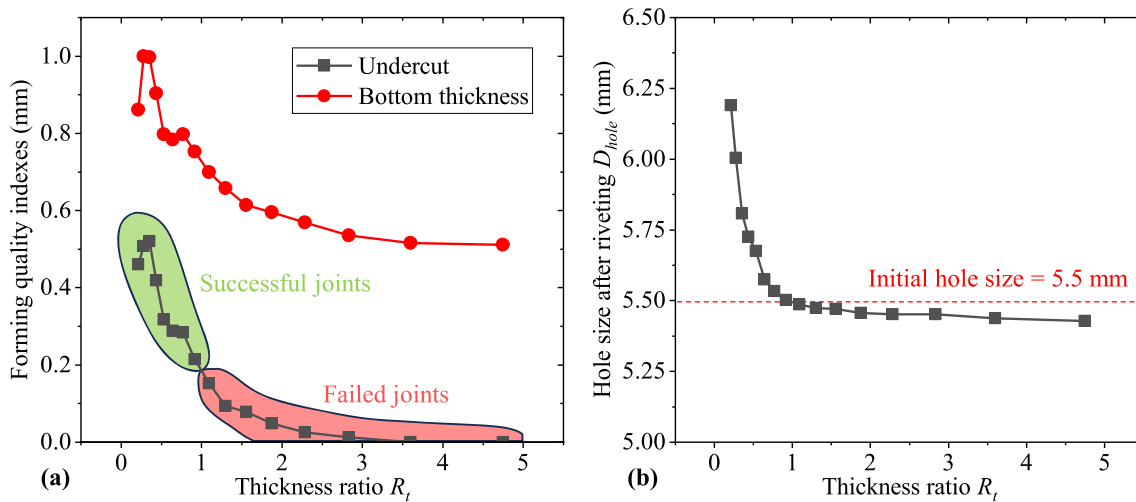


Fig. 25 The effects of varying R_t on (a) the undercut and bottom thickness and (b) the hole size

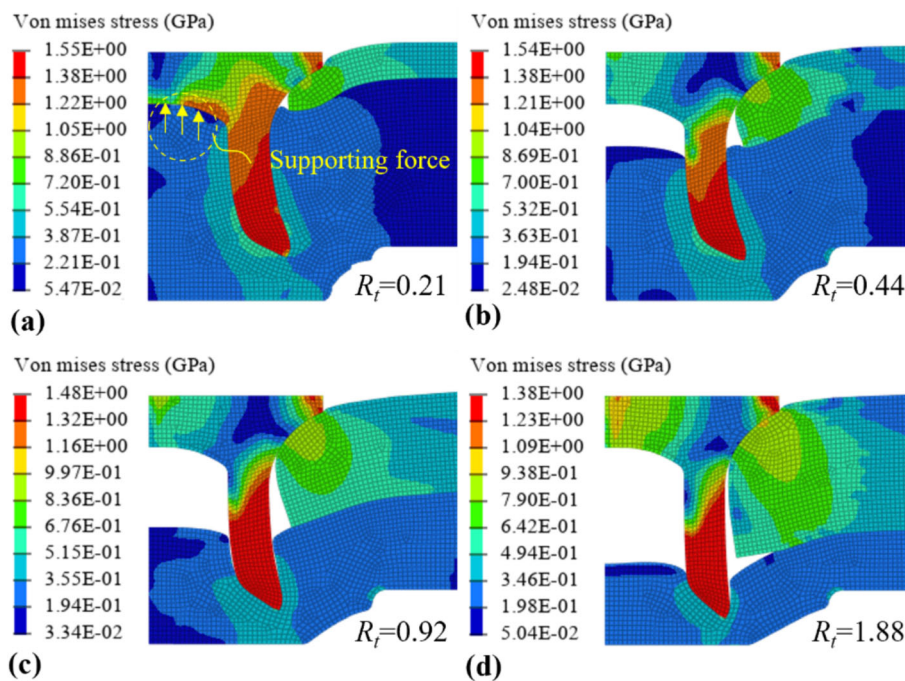


Fig. 26 Distribution of stress of SPR joints: (a) $R_t = 0.21$, (b) $R_t = 0.44$, (c) $R_t = 0.92$, and (d) $R_t = 1.88$

Figure 25 shows the forming quality with different thickness ratios (R_t) when the rivet length is 5.0 mm. To ensure an effective comparison, the other parameters of the rivet and die remain unchanged. It can be observed from Fig. 25(a) that the variation trends of undercut and bottom thickness are basically the same. Both the undercut and bottom thickness gradually increase to the peak when the thickness ratio is smaller than 0.35. However, as the thickness ratio continues to increase, a decreasing trend is observed. This pattern indicates that there is an optimal thickness ratio range where the forming quality is maximized. The bottom thickness of all joints meets the requirements, while the undercut of the joints with a thickness ratio greater than 0.92 is less than 0.2 mm. It can be concluded that a qualified PH-SPR joint can be achieved when the thickness ratio is equal from 0.21 to 0.92. This further

emphasizes the importance of the optimal range for matching the thickness ratio and rivet length in Fig. 24. Additionally, the hole sizes after riveting are smaller than 5.5 mm when the thickness ratio is larger than 1.1, as shown in Fig. 25(b). This reduction in hole size indicates that excessive material deformation occurs at higher thickness ratios.

The simulated cross section profiles with four thickness ratios are selected to observe the differences, as shown in Fig. 26. When the thickness ratio is 0.21 in Fig. 26(a), the material from the bottom sheet fully fills the gap between the rivet head and the bottom sheet, which can provide an upward supporting force to rivet head. This results in the rivet being unable to further flare, and a smaller undercut can be found. When the thickness ratio increases to 0.35, the undercut increases with the decrease in upward force to the rivet head, as

shown in Fig. 26(b). The undercut and the stress on the rivet leg decrease with the increase in top sheet thickness due to the decrease in the length of rivet piercing, while the volume of the gap increases with the increase in top sheet thickness, as shown in Fig. 26(a) to (d). It is difficult to form an effective interlock when the bottom sheet thickness is too small, as shown in Fig. 26(d). Although the bending deformation of the top sheet is small when the thickness ratio is relatively large, the local plastic deformation of the top sheet under the rivet head leads to a decrease in hole size, as shown in Fig. 26(b) to (d).

5. Conclusions

In the present study, a 2D axisymmetric FE model is developed to simulate the PH-SPR process of the steel–aluminum hybrid sheets. The effects of process parameters (e.g., rivet hardness, geometric dimensions of rivet and die, hole size, and material and thickness of sheet) on the joint quality of the PH-SPR joints are investigated. The main conclusions are summarized as follows:

- (1) The undercut increases gradually and decreases slowly after reaching maximum undercut with the increase in yield stress of the rivet, and a decreasing trend is found in the bottom thickness. The rivet with a hardness of H1 is suitable for the bottom sheet with a yield stress of 89 MPa, and the rivet with a hardness of H4 is appropriate for the bottom sheet with a yield stress greater than 165 MPa.
- (2) The increasing rivet length and decreasing die depth can improve the undercut and achieve a bottom thickness that meets the requirement. For a given die diameter, the increase in rivet length leads to the increasing undercut and decreasing bottom thickness.
- (3) The larger hole size can improve the joint quality, and a greater increasing trend in undercut can be observed with the increase in hole size when the top sheet thickness is 0.8 mm. An increasing trend of hole size before and after riveting is observed when the top sheet thickness is 0.8 mm.
- (4) The undercuts of the top sheet thickness of 1.2 mm and 1.6 mm show an increasing trend and a decreasing trend with the increase in bottom sheet material strength, respectively. When the top sheet thickness is 1.6 mm, the undercut decreases with the increase in yield stress of the bottom sheet. In contrast, when the top sheet thickness is 1.2 mm, a higher increasing trend is found in the early stage, followed by a slower increasing trend in the later stage.
- (5) When the thickness ratio exceeds 1.3, no successful joints are observed, and the range of successful joining reduces with the increase in thickness ratio. The minimum and maximum rivet lengths required for a successful joining increase and decrease, respectively, with the increase in thickness ratio. When the rivet length is 5.0 mm, the undercut and bottom thickness increase gradually to the peak when the thickness ratio is smaller than 0.35, and a decreasing trend for two indicators is observed when the thickness ratio increases from 0.44 to 4.75.

Acknowledgments

This work is gratefully acknowledged with financial support from The Guangxi Key R&D Programme (Grant No. AB23026104), The Liuzhou Science and Technology Programme (Grant No. 2023PRJ0102), and The Construction of Guangxi Construction Machinery Low Carbon Digital Intelligence Technology Innovation Centre (Grant No. 2023PRJ0101). All experiments were carried out at Guangxi University of Science and Technology. Prof. Aiguo Cheng and Prof. Youping Sun are acknowledged for their guidance through each stage of the process. I also want to thank the research team members Mrs. Wangzhen Li and Mr. Guojian Luo for their cooperation and assistance in collecting data for my experiment. For this, I am extremely grateful.

References

1. J. Wang, G. Zhang, X. Zheng, J. Li, X. Li, W. Zhu and J. Yanagimoto, A self-piercing riveting method for joining of continuous carbon fiber reinforced composite and aluminum alloy sheets, *Compos. Struct.*, 2021, **259**, p 113219. <https://doi.org/10.1016/j.compstruct.2020.113219>
2. D.F. Wang and S.H. Li, Material selection decision-making method for multi-material lightweight automotive body driven by performance, *Proc. Inst. Mech. Eng. Part. L J. Mat. Des. Appl.*, 2022, **236**(4), p 730–746. <https://doi.org/10.1177/14644207211055661>
3. L. Duan, Z. Du, H. Ma, W. Li, W. Xu and X. Liu, Simplified modelling of self-piercing riveted joints and application in crashworthiness analysis for steel-aluminium hybrid beams, *J. Manuf. Process.*, 2023, **85**, p 948–962. <https://doi.org/10.1016/j.jmapro.2022.11.068>
4. H. Yang and Y. Ren, Crashworthiness design of CFRP/AL hybrid circular tube under lateral crushing, *Thin. Wall. Struct.*, 2023, **186**, p 110669. <https://doi.org/10.1016/j.tws.2023.110669>
5. F. Kappe, C. Zirngibl, B. Schleich, M. Bobbert, S. Wartzack and G. Meschut, Determining the influence of different process parameters on the versatile self-piercing riveting process using numerical methods, *J. Manuf. Process.*, 2022, **84**, p 1438–1448. <https://doi.org/10.1016/j.jmapro.2022.11.019>
6. D. Li, A. Chrysanthou, I. Patel and G. Williams, Self-piercing riveting—a review, *Int. J. Adv. Manuf. Tech.*, 2017, **92**(5–8), p 1777–1824. <https://doi.org/10.1007/s00170-017-0156-x>
7. X. Zhang, X. He, B. Xing, W. Wei and J. Lu, Quasi-static and fatigue characteristics of self-piercing riveted joints in dissimilar aluminium–lithium alloy and titanium sheets, *J. Mater. Res. Technol.*, 2020, **9**(3), p 5699–5711. <https://doi.org/10.1016/j.jmrt.2020.03.095>
8. Y. Liu, W. Zhuang, Y. Luo, D. Xie and W. Mu, Joining mechanism and damage of self-piercing riveted joints in carbon fibre reinforced polymer composites and aluminium alloy, *Thin. Wall. Struct.*, 2023, **182**, p 110233. <https://doi.org/10.1016/j.tws.2022.110233>
9. B. Asati, N. Shajan, V.T.A. Kishore, K.S. Arora and R.G. Narayanan, A comparative investigation on self-piercing riveting and resistance spot welding of automotive grade dissimilar galvanized steel sheets, *Int. J. Adv. Manuf. Tech.*, 2022, **123**(3–4), p 1079–1097. <https://doi.org/10.1007/s00170-022-10226-y>
10. S. Gupta, R. Ganesh Narayanan, S. Das and B. Asati, Joining of dissimilar galvanized steel sheets by resistance spot welding and self-piercing riveting, *Advances in Additive Manufacturing and Metal Joining*, 2023, **24**, p 381–393.
11. R. Haque, Quality of Self-Piercing Riveting (SPR) Joints from Cross-Sectional Perspective: A Review, *Arch. Civ. Mech. Eng.*, 2018, **18**(1), p 83–93. <https://doi.org/10.1016/j.acme.2017.06.003>
12. C. Wang, W. Yu, A. Cheng and Z. He, Effect of Process Parameters on Joint Quality and Mechanical Properties of Local-Thickened self-Piercing Riveted Steel and Die-Casting Aluminum Joints, *Int. J. Adv. Manuf. Tech.*, 2024, **132**, p 5945–5964. <https://doi.org/10.1007/s00170-024-13559-y>
13. C. Wang, Z. Du, A. Cheng, Z. He, H. Tan and W. Yu, Influence of Process Parameters and Heat Treatment on Self-Piercing Riveting of High-Strength Steel and Die-Casting Aluminium, *J. Mater. Res.*

- Technol.*, 2023, **26**, p 8857–8878. <https://doi.org/10.1016/j.jmrt.2023.09.187>
14. Y. Ma, M. Lou, Y. Li and Z. Lin, Effect of Rivet and Die on Self-Piercing Rivetability of AA6061-T6 and Mild Steel CR4 of Different Gauges, *J. Mater. Process. Tech.*, 2018, **251**, p 282–294. <https://doi.org/10.1016/j.jmatprotec.2017.08.020>
 15. H. Jiang, S. Gao, G. Li and J. Cui, Structural Design of Half Hollow Rivet for Electromagnetic Self-Piercing Riveting Process of Dissimilar Materials, *Mater. Design*, 2019, **183**, p 108141. <https://doi.org/10.1016/j.matdes.2019.108141>
 16. B. Asati, R.G. Narayanan, N. Shajan and K.S. Arora, Effect of Die Design and Sheet Placement on Self-Piercing Rivet of Automotive Steels and Comparison with Resistance Spot and Friction Stir Spot Welding, *J. Mater. Eng. Perform.*, 2023, **32**, p 8913–8926. <https://doi.org/10.1007/s11665-022-07762-9>
 17. C. Wang, Z. Du, A. Cheng and Z. He, Numerical Investigation of Joinability and Forming Quality Improvement on Self-Piercing Riveting Process with Varying Sheet Stack Combinations, *Thin. Wall. Struct.*, 2024, **201**, p 112017. <https://doi.org/10.1016/j.tws.2024.112017>
 18. Y. Ma, S. Niu, H. Shan, Y. Li and N. Ma, Impact of Stack Orientation on Self-Piercing Riveted and Friction Self-Piercing Riveted Aluminum alloy and Magnesium Alloy Joints, *Automotive Innov.*, 2020, **3**(3), p 242–249. <https://doi.org/10.1007/s42154-020-00108-y>
 19. K. Mori, Y. Abe and T. Kato, Self-Pierce Riveting of Multiple Steel and Aluminium Alloy Sheets, *J. Mater. Process. Tech.*, 2014, **214**(10), p 2002–2008. <https://doi.org/10.1016/j.jmatprotec.2013.09.007>
 20. Y. Abe, T. Kato and K. Mori, Joinability of Aluminium alloy and Mild Steel Sheets by Self Piercing Rivet, *J. Mater. Process. Tech.*, 2006, **177**(1–3), p 417–421. <https://doi.org/10.1016/j.jmatprotec.2006.04.029>
 21. X. He, B. Xing, K. Zeng, F. Gu and A. Ball, Numerical and Experimental Investigations of Self-Piercing Riveting, *Int. J. Adv. Manuf. Tech.*, 2013, **69**(1–4), p 715–721. <https://doi.org/10.1007/s00170-013-5072-0>
 22. Z. Du, L. Duan, L. Jing, A. Cheng and Z. He, Numerical Simulation and Parametric Study on Self-Piercing Riveting Process of Aluminium-Steel Hybrid Sheets, *Thin. Wall. Struct.*, 2021, **164**, p 107872. <https://doi.org/10.1016/j.tws.2021.107872>
 23. H. Zhao, L. Han, Y. Liu and X. Liu, Analysis of Joint Formation Mechanisms for Self-Piercing Riveting (SPR) Process with Varying Joining Parameters, *J. Manuf. Process.*, 2022, **73**, p 668–685. <https://doi.org/10.1016/j.jmapro.2021.11.038>
 24. H.Q. Ang, An Overview of Self-Piercing Riveting Process with Focus on Joint Failures, Corrosion Issues and Optimisation Techniques, *Chin. J. Mech. Eng-En.*, 2021, **34**(1), p 1–25. <https://doi.org/10.1186/s10033-020-00526-3>
 25. Y. Abe, T. Kato and K. Mori, Self-Piercing Riveting of High Tensile Strength Steel and Aluminium Alloy Sheets Using Conventional Rivet and Die, *J. Mater. Process. Tech.*, 2009, **209**(8), p 3914–3922. <https://doi.org/10.1016/j.jmatprotec.2008.09.007>
 26. B. Uhe, C.M. Kuball, M. Merklein and G. Meschut, Improvement of a Rivet Geometry for the Self-Piercing Riveting of High-Strength Steel and Multi-Material Joints, *Prod. Eng.*, 2020, **14**(4), p 417–423. <https://doi.org/10.1007/s11740-020-00973-w>
 27. L. Deng, M. Lou, Y. Li and B.E. Carlson, Thermally Assisted Self-Piercing Riveting of AA6061-T6 to Ultrahigh Strength Steel, *J. Manuf. Sci. E-T. Asme.*, 2019, **141**(10), p 101006. <https://doi.org/10.1115/1.4044255>
 28. Y. Zhang, R. Yi, P. Wang, C. Fu, N. Cai and J. Ju, Self-piercing Riveting of Hot Stamped Steel and Aluminum Alloy Sheets Base on local softening zone, *Steel Res. Int.*, 2021, **92**(4), p 2000535. <https://doi.org/10.1002/srin.202000535>
 29. Y. Ma, B. Yang, S. Hu, H. Shan, P. Geng, Y. Li and N. Ma, Combined Strengthening Mechanism of Solid-State Bonding and Mechanical Interlocking in Friction Self-Piercing Riveted AA7075-T6 Aluminum Alloy Joints, *J. Mater. Sci. Technol.*, 2022, **105**, p 109–121. <https://doi.org/10.1016/j.jmst.2021.07.026>
 30. X. Zhang, X. He, B. Xing, W. Wei and J. Lu, Pre-holed Self-Piercing Riveting of Carbon Fibre Reinforced Polymer Laminates and Commercially Pure Titanium Sheets, *J. Mater. Process. Tech.*, 2020, **279**, p 116550. <https://doi.org/10.1016/j.jmatprotec.2019.116550>
 31. C. Wang, W. Yu, A. Cheng and Z. He, Study on the Failure Mechanism and Mechanical Properties of Multi-Layer Hole-Drilled Self-Piercing Riveted Three-Layer Steel/Aluminum Hybrid Joints, *Eng. Fail. Anal.*, 2024, **164**, p 108681. <https://doi.org/10.1016/j.engfailanal.2024.108681>
 32. A. Cheng, C. Wang, Y. Sun and G. Luo, Effects of Hole Sizes and Stack Thicknesses on Mechanical Properties and Failure Behavior of Pre-Holed self-Piercing Riveted Steel-Aluminum Joints, *J. Mater. Eng. Perform.*, 2024 <https://doi.org/10.1007/s11665-024-09767-y>
 33. T. Tran, S. Hou, X. Han and M. Chau, Crushing Analysis and Numerical Optimization of Angle Element Structures Under Axial Impact Loading, *Compos. Struct.*, 2015, **119**, p 422–435. <https://doi.org/10.1016/j.compstruct.2014.09.019>
 34. H. Zhao, L. Han, Y. Liu and X. Liu, Modelling and Interaction Analysis of the Self-Pierce Riveting Process Using Regression Analysis and FEA, *Int. J. Adv. Manuf. Tech.*, 2021, **113**(1–2), p 159–176. <https://doi.org/10.1007/s00170-020-06519-9>

Publisher's Note Springer Nature remains neutral with regard to jurisdictional claims in published maps and institutional affiliations.

Springer Nature or its licensor (e.g. a society or other partner) holds exclusive rights to this article under a publishing agreement with the author(s) or other rightsholder(s); author self-archiving of the accepted manuscript version of this article is solely governed by the terms of such publishing agreement and applicable law.